Angewandte Chemie
Eine Zeitschrift der Gesellschaft Deutscher Chemiker

Supporting Information

Coupling Manipulation of Interfacial Chemistry and Coordination Structure in Vanadium Oxides Enables Rapid Magnesium Ion Diffusion Kinetics

*W. Wang, W. Wang, F. Xiong, J. Meng, J. Wu, W. Yang, J. Long, J. Chen, J. Chen, Q. An**

Supporting Information

Coupling Manipulation of Interfacial Chemistry and Coordination Structure in Vanadium Oxides Enables Rapid Magnesium Ion Diffusion Kinetics

Weixiao Wang,[a] Wenwen Wang,[a] Fangyu Xiong,[b] Jiashen Meng,[a] Jinsong Wu,[a] Wei Yang,[a] Juncai Long,[a] Jinghui Chen,[a] Jiajun Chen,[a] and Qinyou An*[a]

[a] W. Wang, W. Wang, J. Meng, J. Wu, W. Yang, J. Long, J. Chen, J. Chen, and Prof. Q. An
State Key Laboratory of Advanced Technology for Materials Synthesis and Processing,
Wuhan University of Technology, Wuhan 430070, China
E-mail: anqinyou86@whut.edu.cn

[b] Prof. F. Xiong,
College of Materials Science and Engineering, Chongqing University, Chongqing 400030, China

Experimental Section

Synthesis of Atomically-Thin V_2O_5 Nanosheets

0.864 g commercial V_2O_5 powders (Aladdin, 99.0%) were dissolved in 63 mL deionized water. Afterwards, 12 ml H_2O_2 solution (30 %) was added in the mixed solution under sonication to form a homogeneous yellow solution. Then, the solution was transferred into a 100 mL Teflonlined stainless-steel autoclave and kept at 180 °C for 24 h. Finally, the atomically-thin V_2O_5 nanosheets was obtained after freeze-drying.

Material Characterizations

The morphology of the samples was characterized using field-emission scanning electron microscopy (SEM, JSM-7100F) and transmission electron microscopy (TEM, JEM-1400Plus). X-ray diffraction (XRD, Bruker D8 Discover), Raman spectrometry (LabRAM HR-Evolution, 532 nm) and X-ray photoelectron spectroscopy (XPS, AXIS SUPRA) were carried out to investigate the structure and chemical composition of the samples. The Xray absorption spectroscopy (XAS) spectra at the V K edge were measured at the X-ray absorption station (beamline 1W2B) of the Beijing Synchrotron Radiation Facility (BSRF) in China using a double crystal Si (111) monochromator. Additionally, the in-situ XRD, in-situ Raman and ex-situ XPS spectra were also performed to analyze the electrochemical evolution processes of GAVOH during battery charging and discharging. The elements distribution was acquired by time-of-flight secondary-ion mass spectrometry (TOF-SIMS, nano TOFIII).

Electrochemical Measurements

The cathode was prepared by coating on carbon paper (~ 0.5 mm thickness) with a homogeneous slurry of 70% V_2O_5, 20% acetylene black and 10% PVDF binder in NMP solvent. The half battery was measured using CR2016 coin cell with obtained cathode and active carbon cloth as counter electrode and glass fiber papers as separators (diameter of 17 mm, Whatman GF/A) and 0.2 M $Mg(TFSI)_2$ solution as electrolyte under ambient conditions. Then, the full battery was assembled using CR2016 coin

cell, in which Mg foil with a thickness of 50 μm, glass fiber membrane (Whatman GF/A) and MTB solution were utilized as the anode, separator and electrolyte, respectively. The MTB solution is composed of 1.290 g $Mg(CF_3SO_3)_2$, 0.762 g $MgCl_2$, and 1.067 g $AlCl_3$ dissolved in 20 ml of 1,2-dimethoxyethane (DME). In addition, the interdigital micro-RMBs were assembled, in which L-V_2O_5 as the cathode, Mg foil as the anode, and MTB solution as the electrolyte. All the electrochemical measurements including cyclic voltammetry (CV), galvanostatic charge-discharge (GCD), electrochemical impedance spectroscopy (EIS) and galvanostatic intermittent titration technique (GITT) were conducted with LAND battery testing systems and electrochemical workstation (CHI660E).

DFT Calculations

The first-principles calculations were conducted using the projector-augmented plane-wave method within the framework of density functional theory, implemented in the Vienna ab initio simulation package. The exchange-correlation potential is determined using the generalized gradient approximation as proposed by Perdew, Burke, and Ernzerhof. The long-range van der Waals interaction is accounted for by the DFT-D3 approach. The B-V_2O_5 (110) surface consists of 24 V and 60 O atoms, while the L-V_2O_5 (001) surface comprises 32 V and 80 O atoms. The cut-off energy for plane waves is established at 500 eV. Spin polarization is taken into account in the calculations. The convergence criteria for ionic and electronic optimizations are set to 0.03 eV/Å and 1×10^{-5} eV, respectively. Brillouin zone integration is conducted using a 2×2×1 k-mesh.

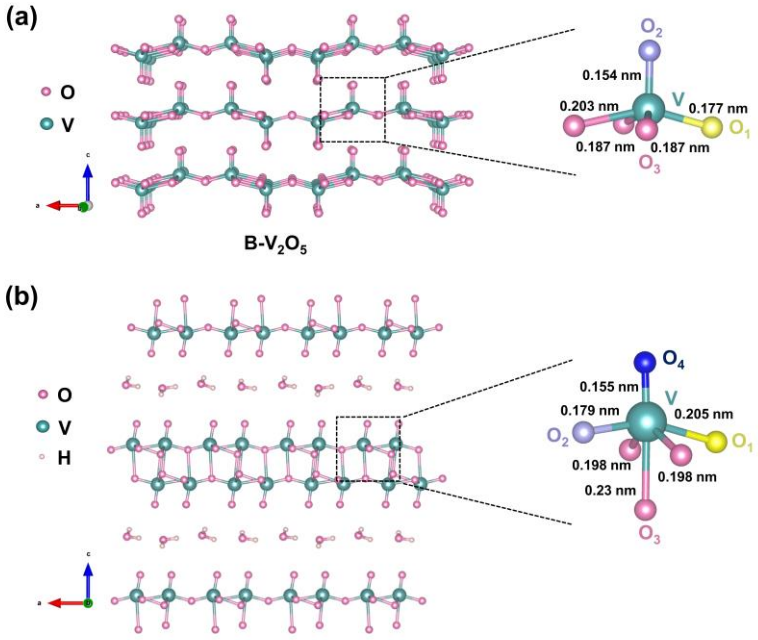

Figure S1. The crystal structure of (a) B-V_2O_5 composed of VO_5 square pyramid, and (b) L-V_2O_5 composed of VO_6 octahedron.

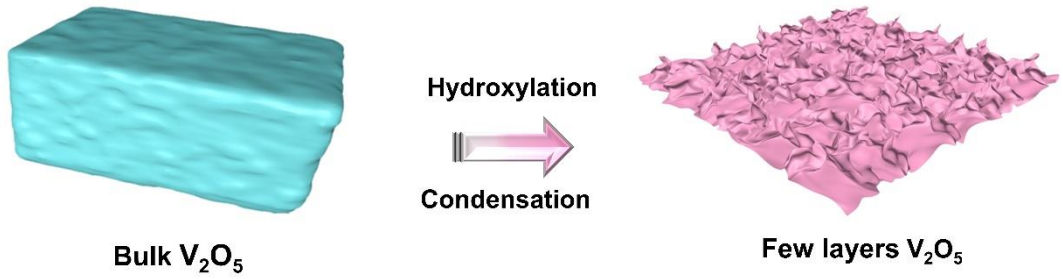

Figure S2. Schematic diagram of the structure arrangement process of layered V_2O_5.

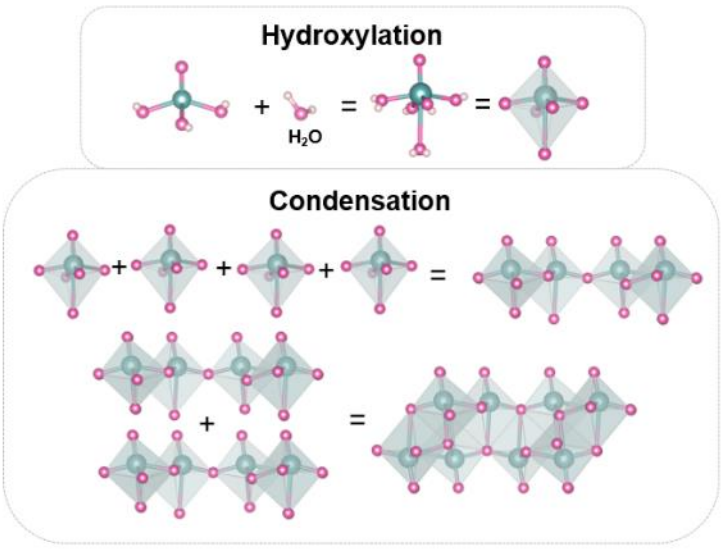

Figure S3. The hydroxylation and condensation mechanism of L-V_2O_5.

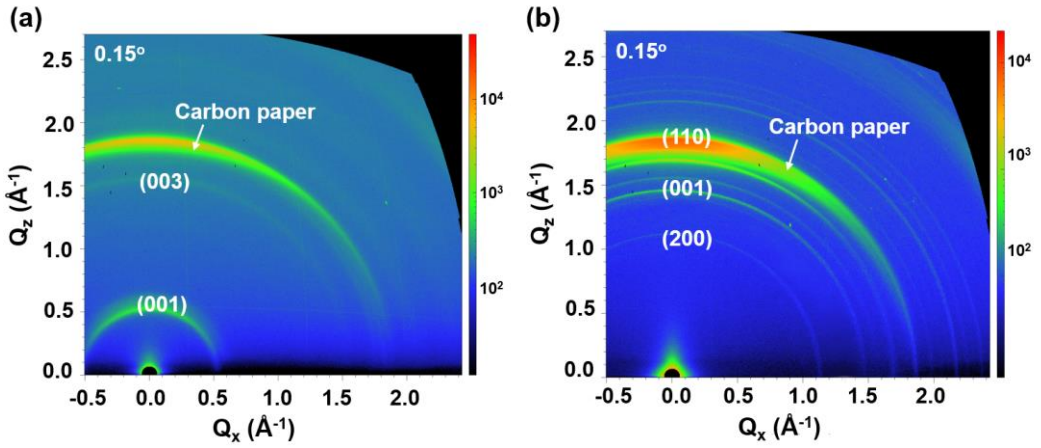

Figure S4. GIWAXS pattern of the (a) L-V_2O_5 electrode and (b) B-V_2O_5 electrode with carbon paper current collector.

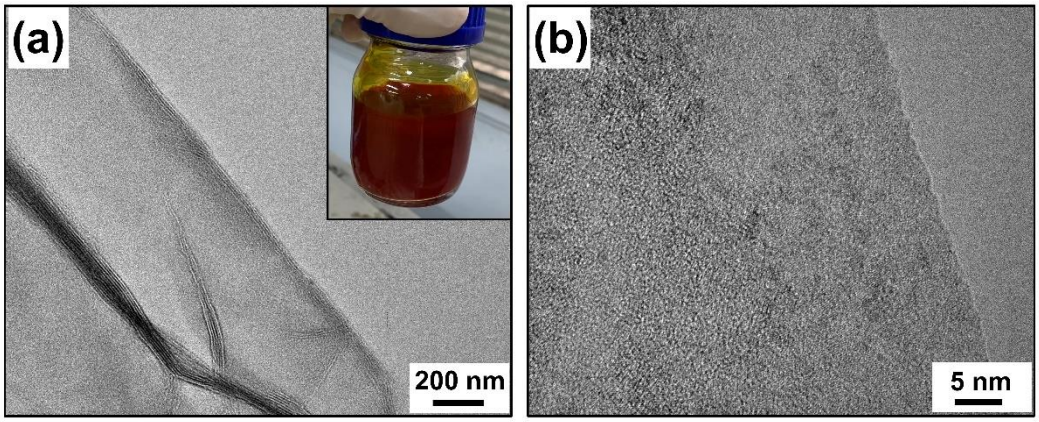

Figure S5. (a) The TEM images, and (d) HRTEM image of L-V_2O_5.

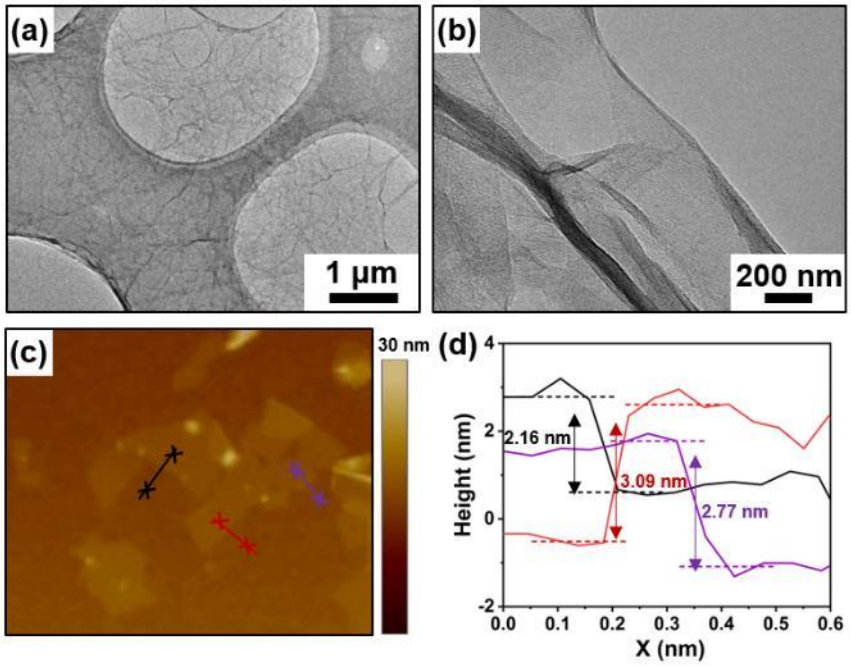

Figure S6. (a, b) TEM images, and (c, b) AFM image of L-V_2O_5.

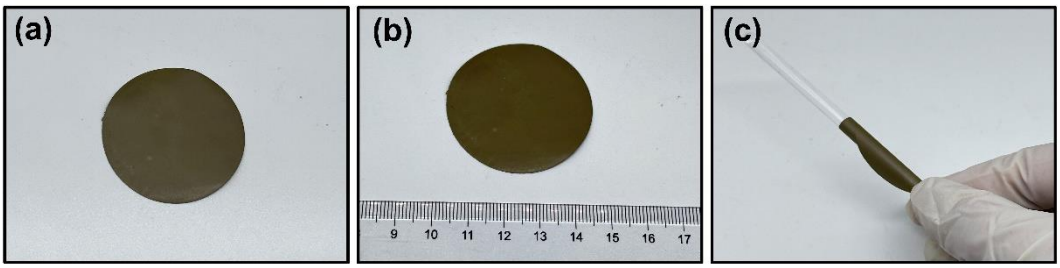

Figure S7. Digital photographs of the flexible L-V_2O_5 film.

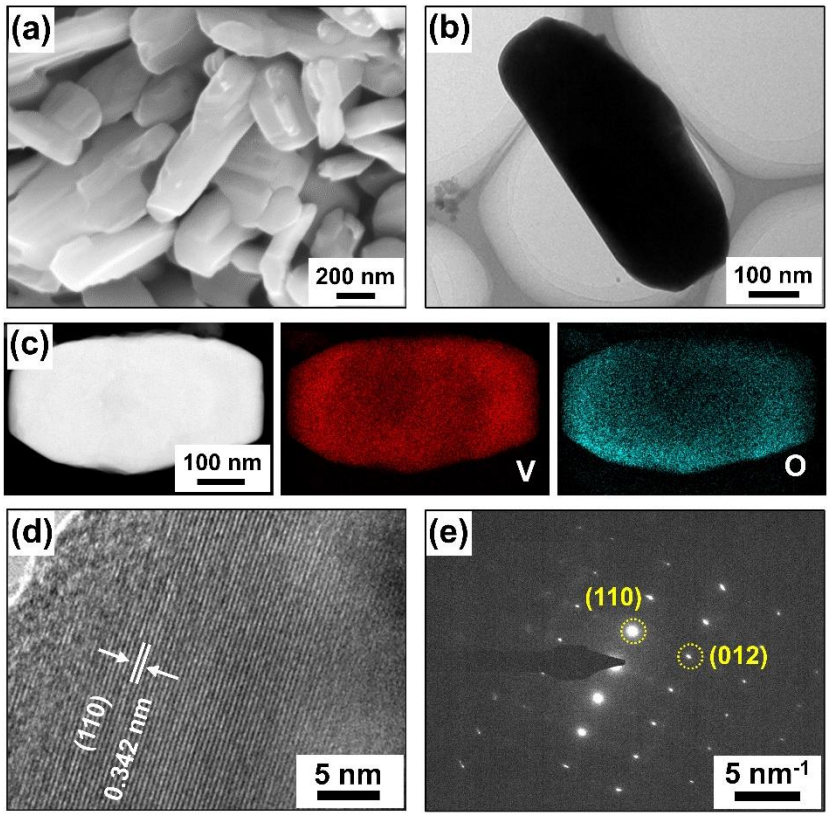

Figure S8. (a) SEM image, (b) TEM image, (c) EDS mapping images, (d) HRTEM image, (e) SAED image of B-V_2O_5.

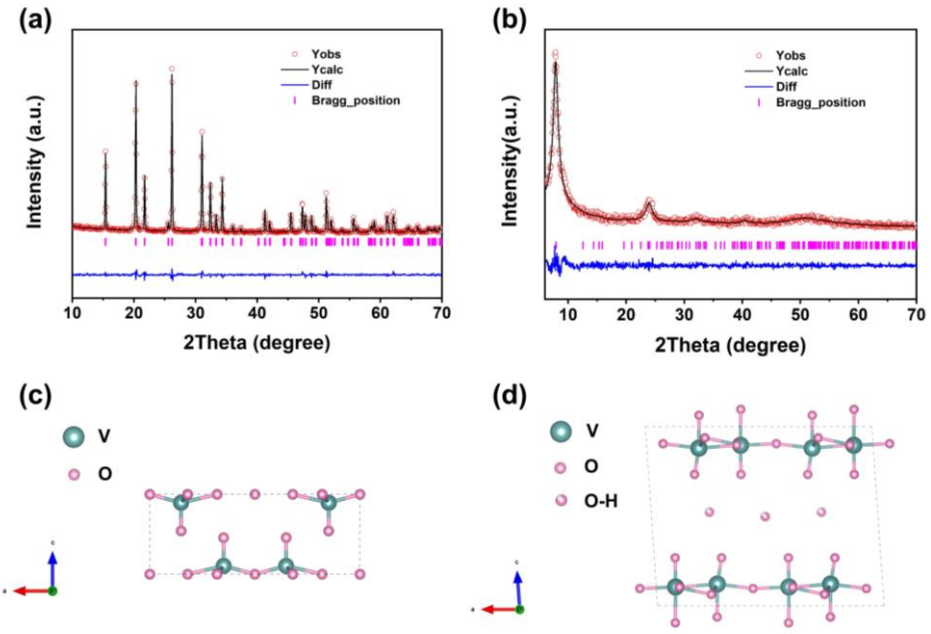

Figure S9. Powder X-ray Rietveld refinement profile for (a) B-V_2O_5 and (b) L-V_2O_5. The structural illustrations of (c) B-V_2O_5 and (d) L-V_2O_5 along a-axis.

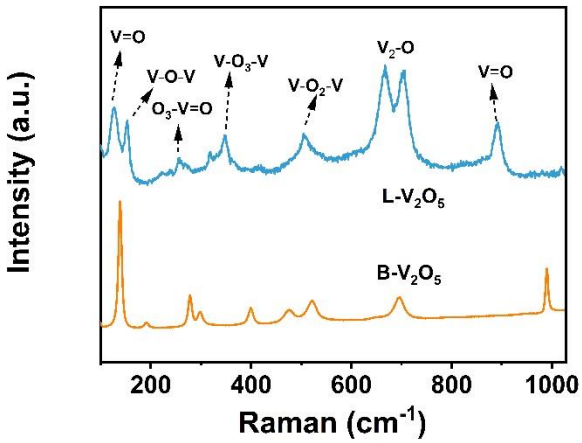

Figure S10. Raman spectra of B-V_2O_5 and L-V_2O_5.

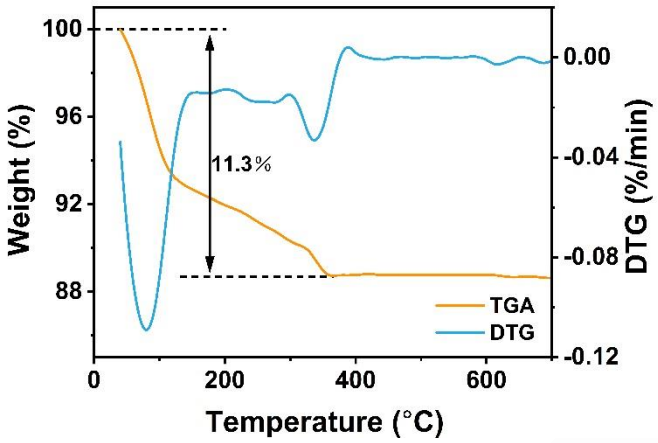

Figure S11. TG and DTG curves of B-V_2O_5 and L-V_2O_5.

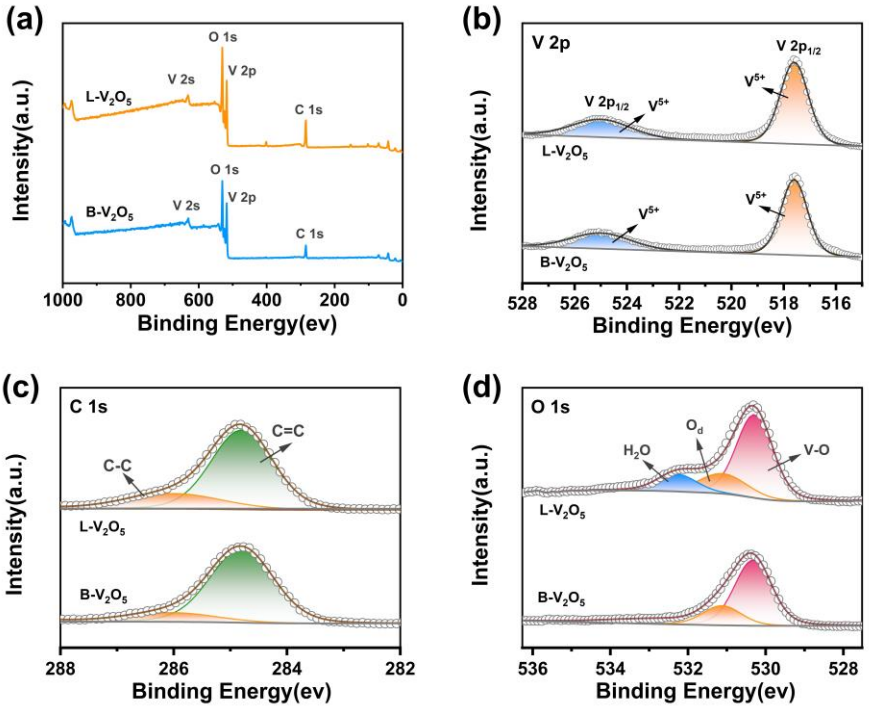

Figure S12. (a) XPS survey spectra, (b) V 2p XPS spectra, (c) C 1s XPS spectra, and (d) O 1s XPS spectra of B-V_2O_5 and L-V_2O_5.

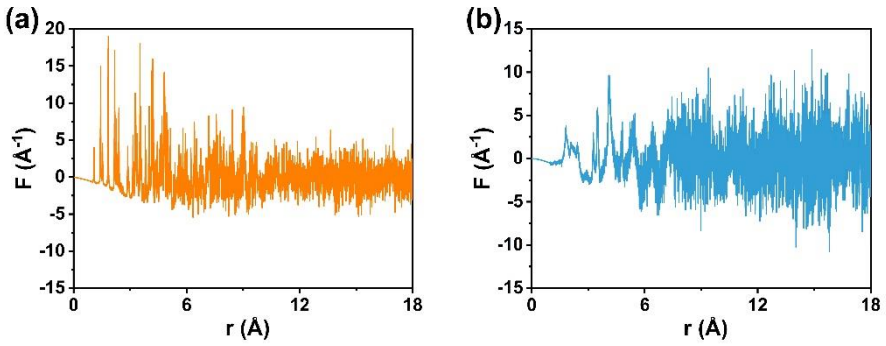

Figure S13. PDF curves of B-V_2O_5 and L-V_2O_5.

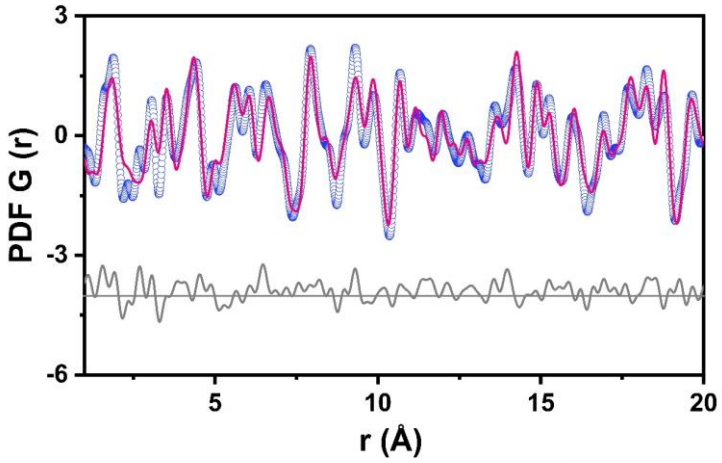

Figure S14. Experimental and fitted PDFs curves of B-V_2O_5.

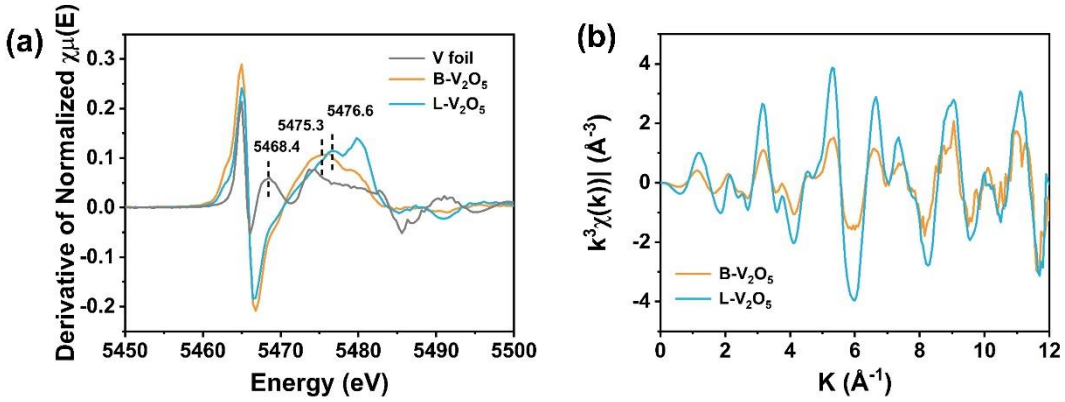

Figure S15. (a) The normalizer XANES spectra, and (b) k^3-weighted EXAFS spectra of B-V_2O_5 and L-V_2O_5.

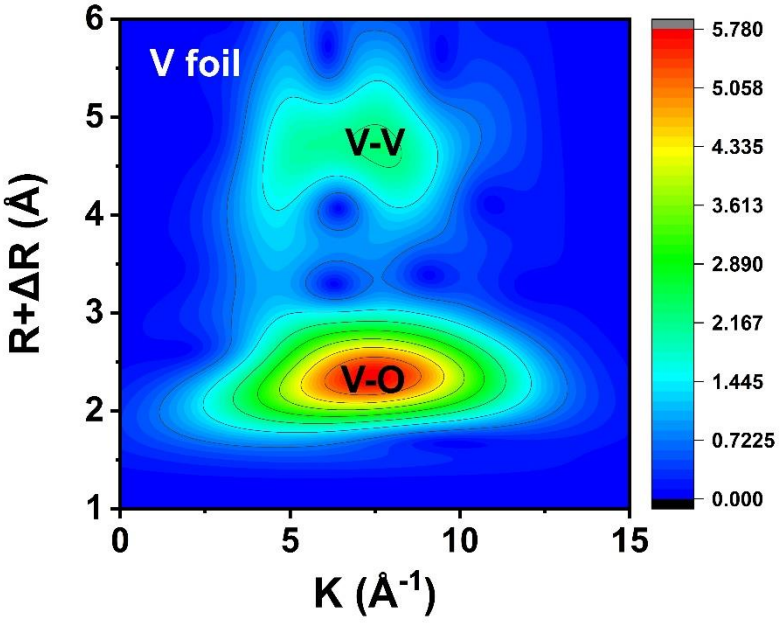

Figure S16. The WT-EXAFS spectra of the V foil.

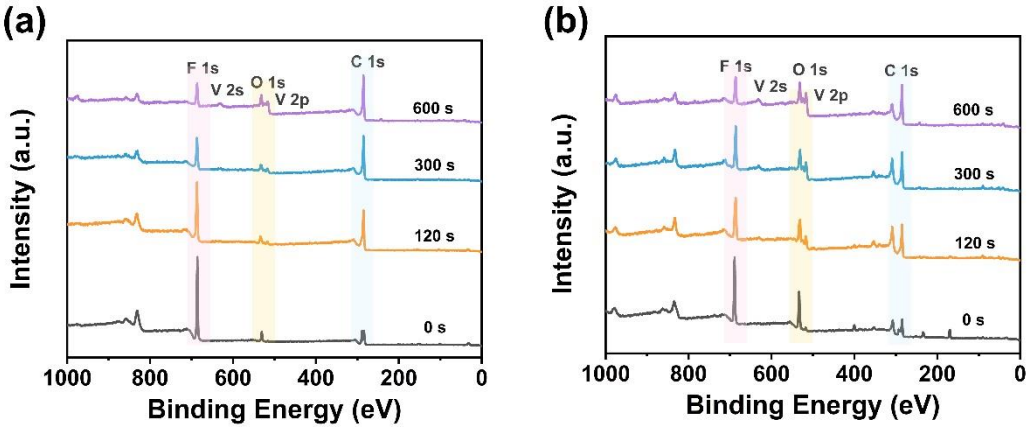

Figure S17. The XPS survey spectra of (a) L-V_2O_5 and (b) B-V_2O_5 electrode after 30 cycles charging/discharging process.

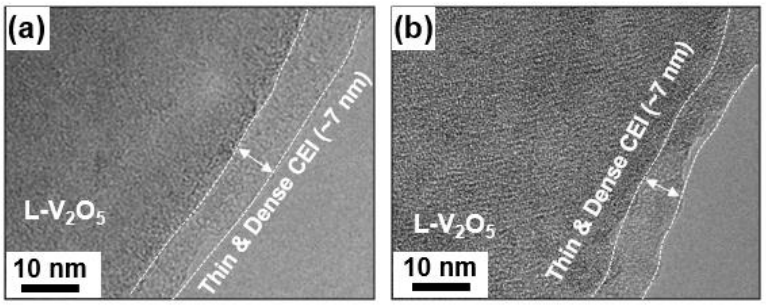

Figure S18. (a, b) TEM images of the L-V_2O_5 electrode after 30 cycles.

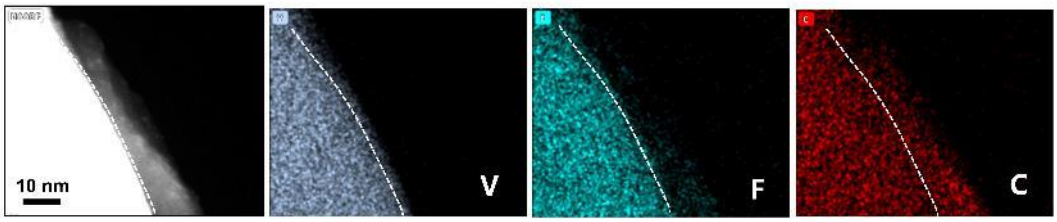

Figure S19. The STEM-EDS images of B-V_2O_5 electrode after 30 cycles.

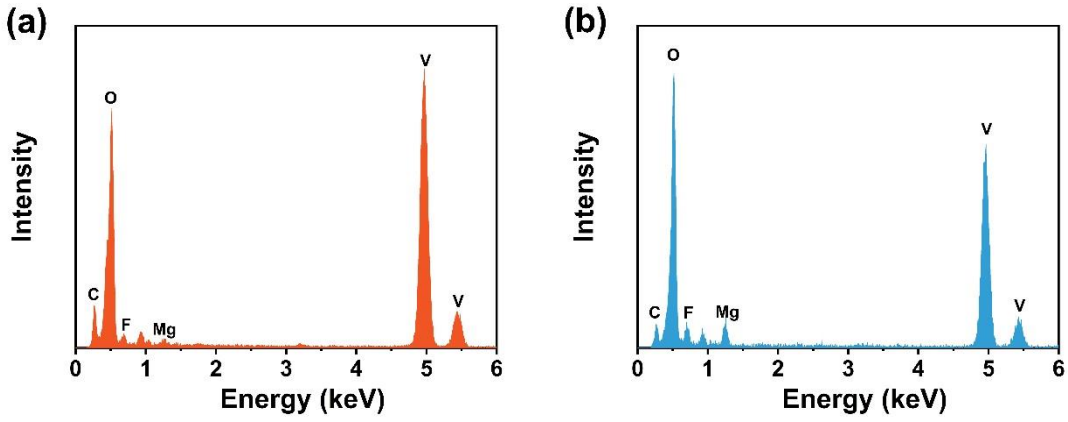

Figure S20. EDS spectra of (a) B-V_2O_5 and (b) L-V_2O_5 electrodes after 30 cycles.

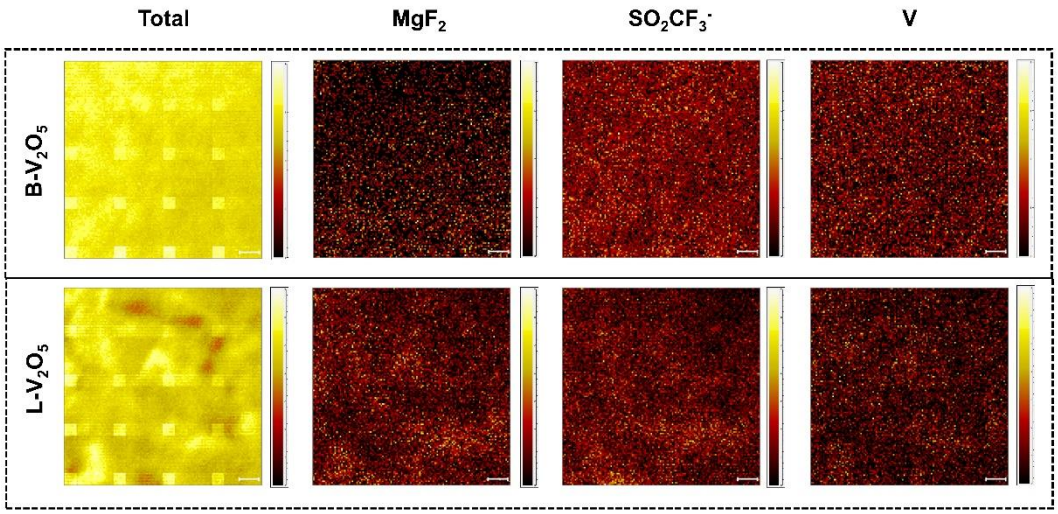

Figure S21. TOF-SIMS images of CEI components of B-V_2O_5 and L-V_2O_5 electrode.

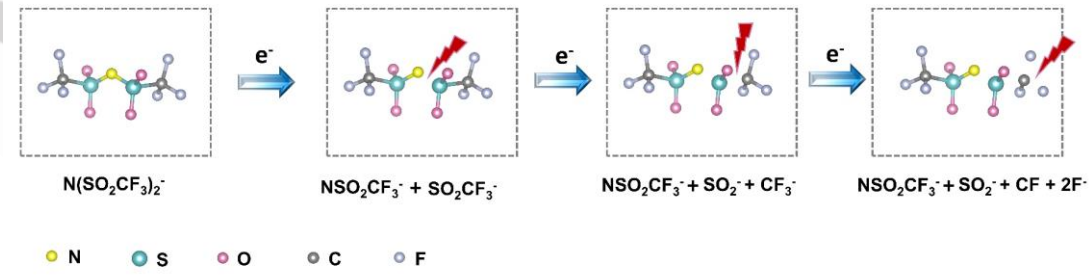

Figure S22. The decomposition mechanism of Mg bis(trifluoromethanesulfonyl)imide anions.

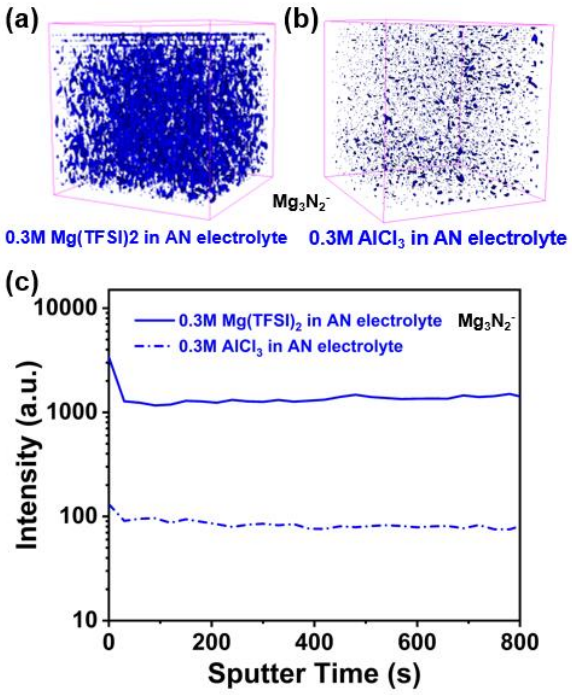

Figure S23. (a, b) The TOF-SIMS 3D views and (c) depth profiles of the $Mg_3N_2^-$ ionic fragments on the surface of L-V_2O_5 electrode during cycling in 0.3M $AlCl_3$/AN electrolyte and 0.3M $Mg(TFSI)_2$/AN electrolyte.

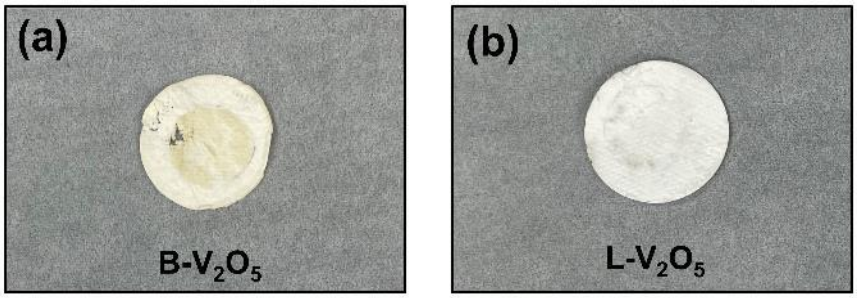

Figure S24. Digital photographs of glass fiber membrane on the B-V_2O_5 and L-V_2O_5 electrodes after 100 cycles.

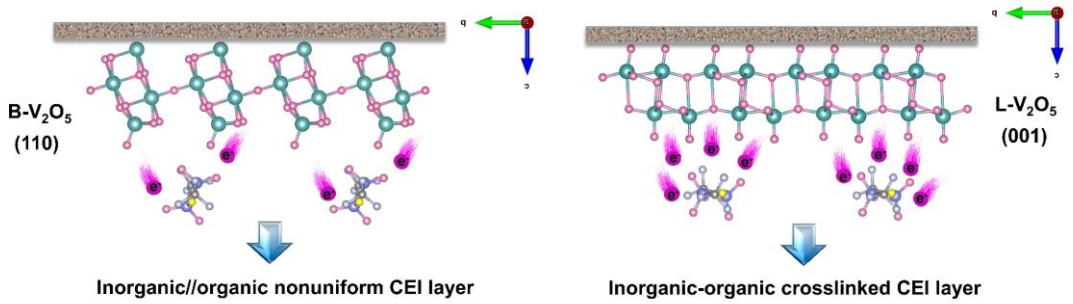

Figure S25. Schematic diagram of CEI layer on B-V_2O_5 and L-V_2O_5 electrode.

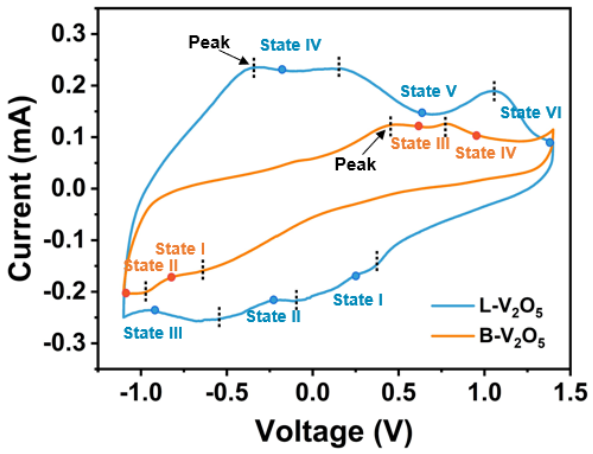

Figure S26. CV curves of B-V_2O_5 and L-V_2O_5 electrodes.

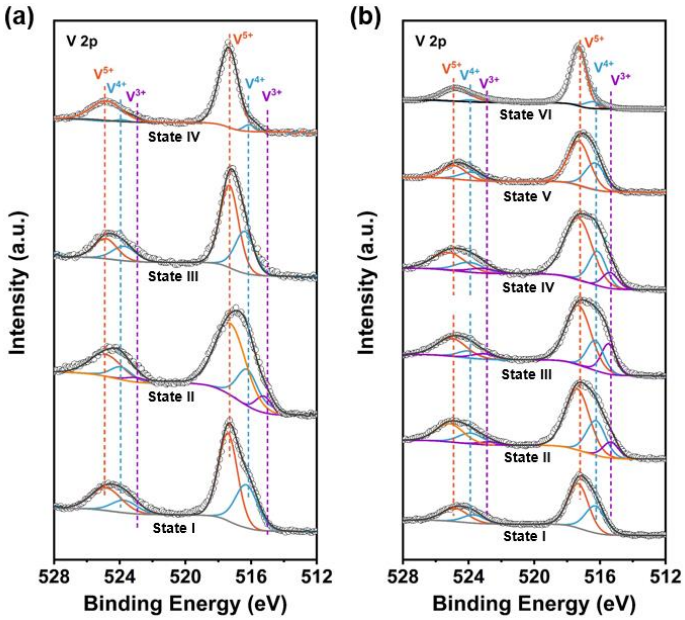

Figure S27. (a, b) The ex-situ V 2p XPS spectra of B-V_2O_5 electrode and L-V_2O_5 electrode at different discharged and charged states.

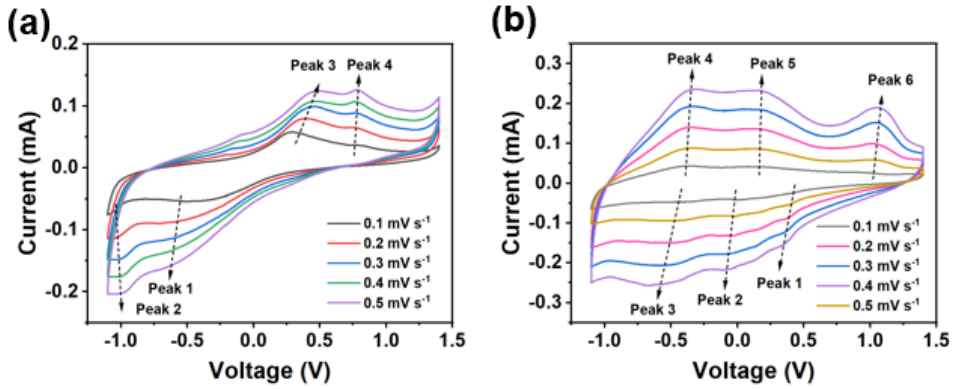

Figure S28. a, b) CV curves, and d, e) the corresponding calculated b values of B-V_2O_5 and L-V_2O_5.

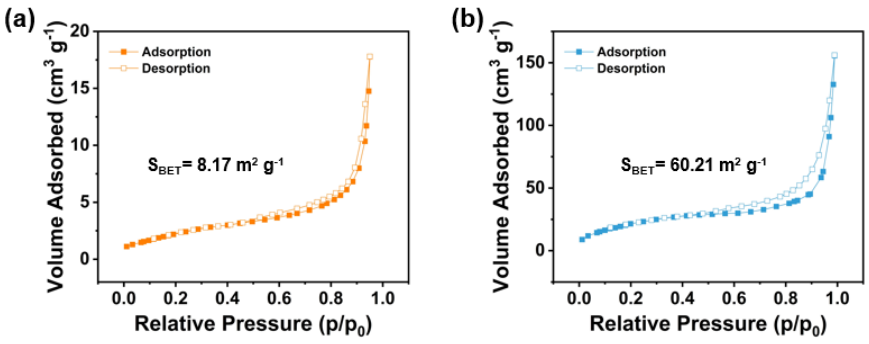

Figure S29. N_2 adsorption-desorption isotherms of a) B-V_2O_5, and b) L-V_2O_5.

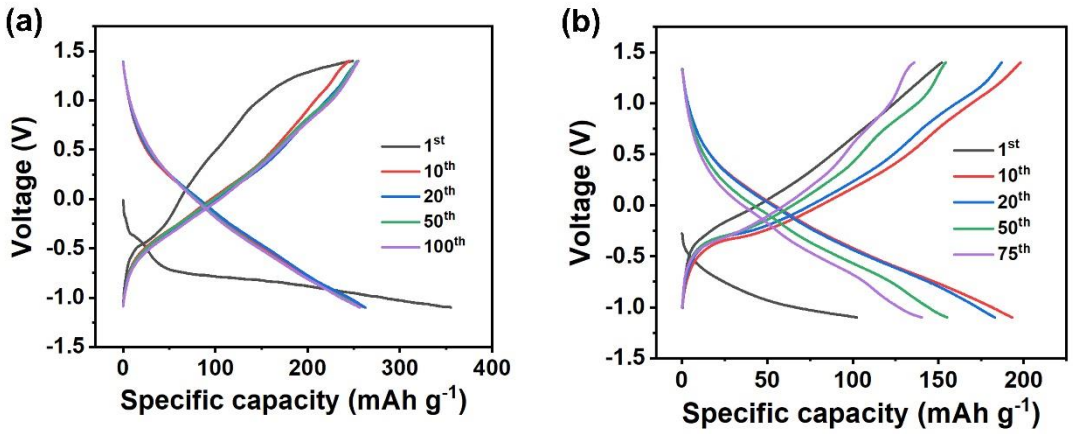

Figure S30. Charge/discharge curves at different cycles of (a) B-V_2O_5 and (b) L-V_2O_5 electrode.

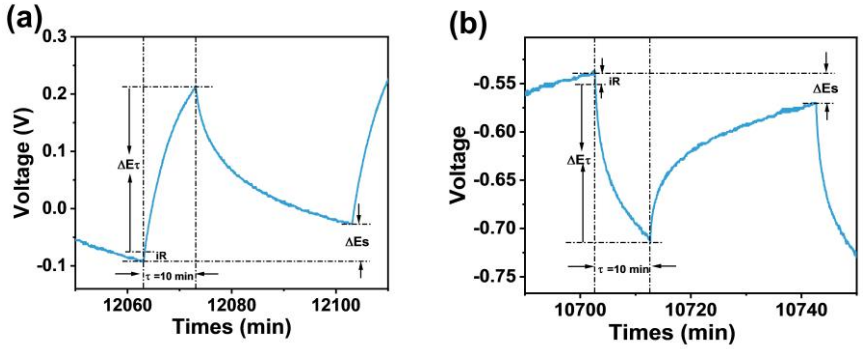

Figure S31. Schematic of charging steps and discharging steps in the GITT profile.

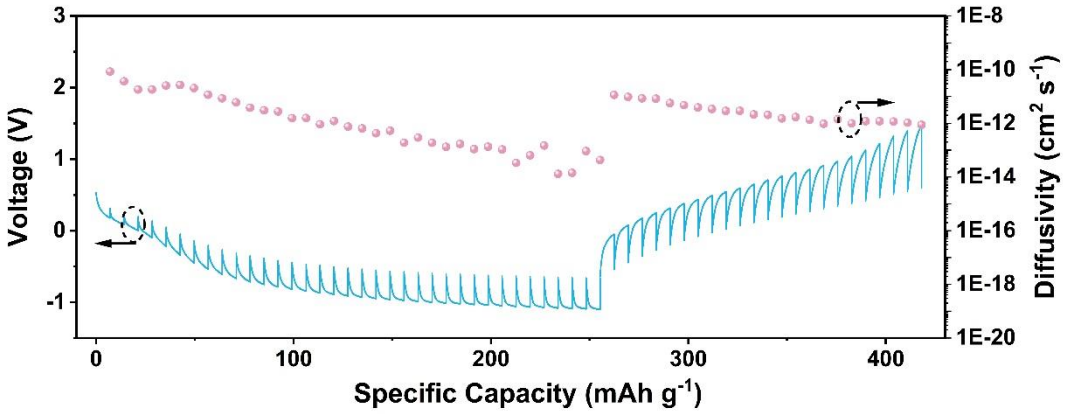

Figure S32. GITT curve and calculated Mg^{2+} diffusion coefficients of B-V_2O_5 electrode.

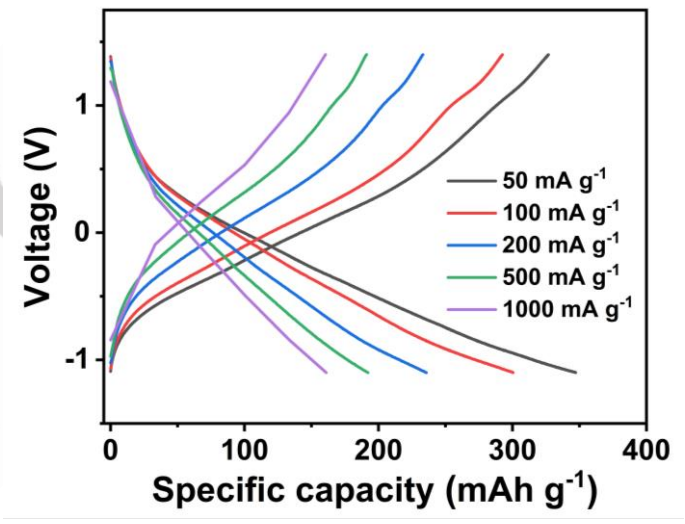

Figure S33. Charge/discharge curves at different current densities of L-V_2O_5 electrode.

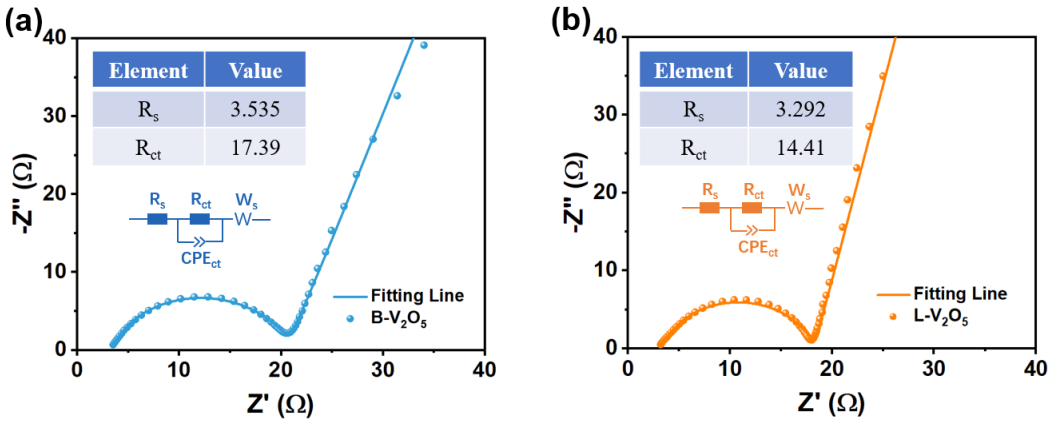

Figure S34. The Nyquist plots and the corresponding fitting parameter (Rct) of the (a) B-V_2O_5 and (b) L-V_2O_5 electrode.

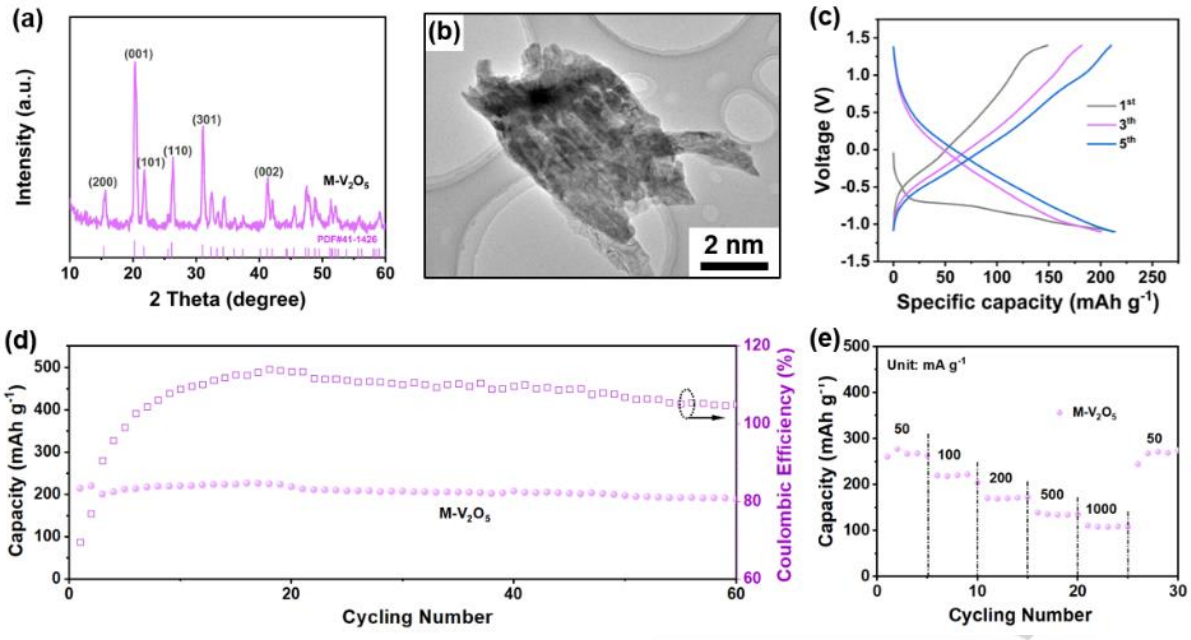

Figure S35. (a) XRD patterns, (b) TEM image, (c) GCD curves, (d) cycling performances, and (e) rate capability at 0.05-1 A g^{-1} of the M-V_2O_5 electrode.

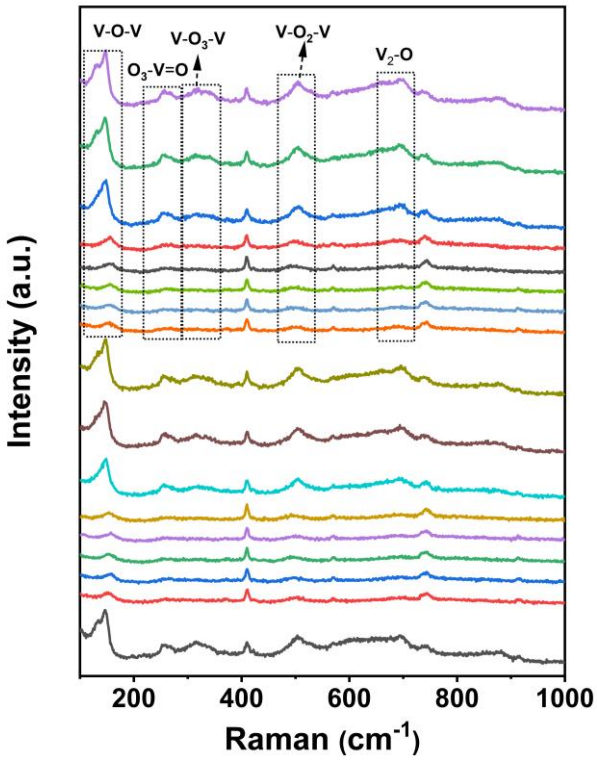

Figure S36. In situ Raman spectra of L-V_2O_5 electrode.

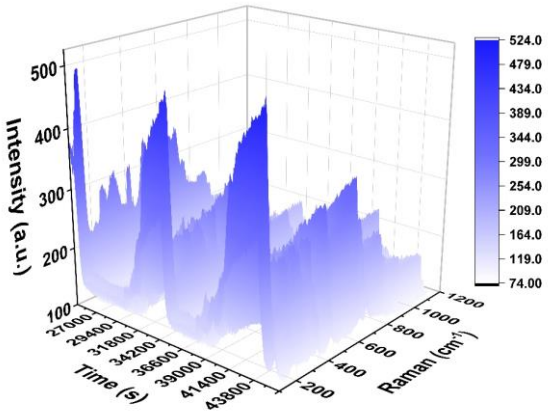

Figure S37. In situ 3D Raman spectra of L-V_2O_5 electrode.

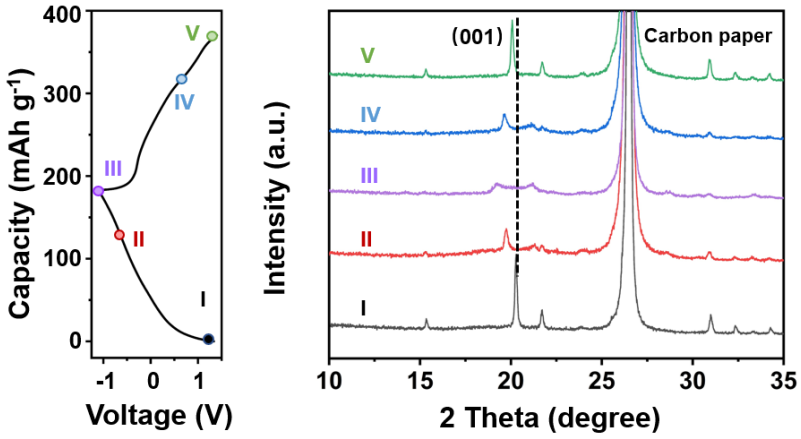

Figure S38. The GCD profile and ex-situ XRD patterns of the B-V_2O_5 electrode.

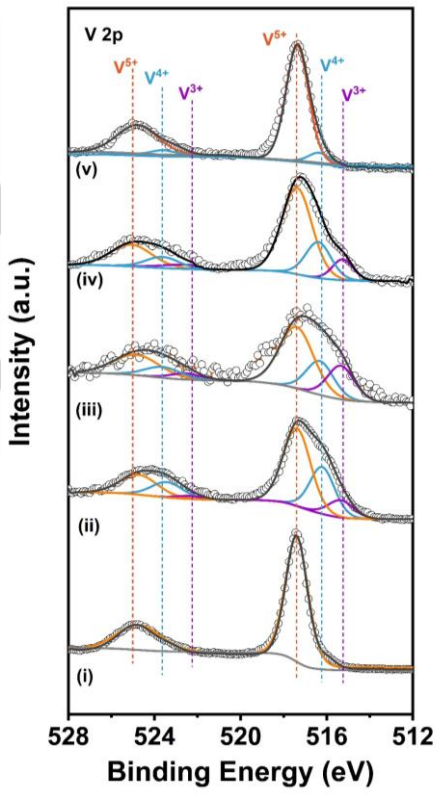

Figure S39. The ex-situ V 2p XPS spectra of L-V_2O_5 electrode at different discharged and charged states.

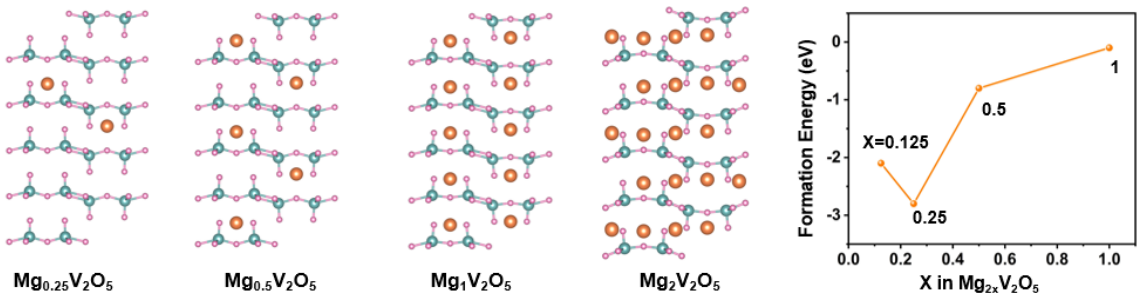

Figure S40. Crystal structure models and the corresponding formation energy of five layers $Mg_{2x}V_2O_5$ (bulk).

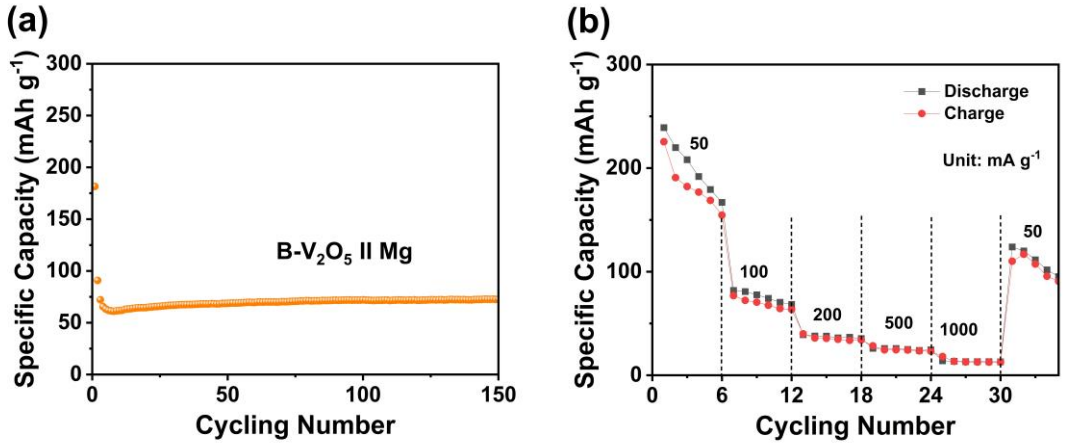

Figure S41. (a) Cycling performances at 0.1 A g^{-1} of B-V_2O_5 electrode. (b) Rate capability at 0.05-1 A g^{-1} of B-V_2O_5 electrode.

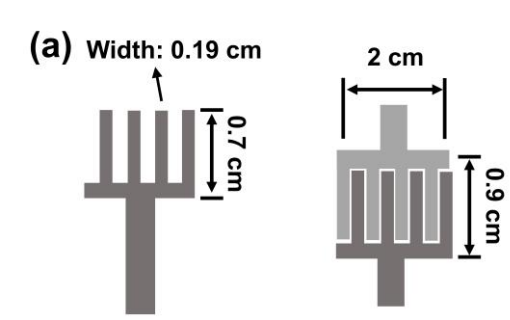

Figure S42. Schematic illustration of L-V_2O_5//Mg interdigital microdevice model.

Table S1. The powder XRD Rietveld refinement results of B-V_2O_5 in terms of crystal system, space group, unit cell and positional parameters.

Crystal System	**Orthorhombic**
Space Group	*Pmmn*
Lattice Parameter	a=11.5138 Å, b=3.5648 Å, c=4.3745 Å α = β = γ = 90°

Atom	**x**	**y**	**z**	**Occ.**
V1	0.10060	0.25000	0.89340	1.000
O1	0.10430	0.25000	0.53600	1.000
O2	-0.06940	0.25000	0.00340	1.000
O3	0.25000	0.25000	0.00200	1.000

* Rwp = 5.85%, Rp = 4.67%

Table S2. The powder XRD Rietveld refinement results of L-V_2O_5 in terms of crystal system, space group, unit cell and positional parameters.

Crystal System	**Orthorhombic**			
Space Group	*C2/m*			
Lattice Parameter	a=14.1205 Å, b=4.1113 Å, c=11.1892 Å α =γ = 90°, β = 86.078°			
Atom	**x**	**y**	**z**	**Occ.**
V1	0.91467	0.00000	0.10463	1.000
V2	0.41467	0.50000	0.10463	1.000
V3	0.22992	0.00000	0.12078	1.000
V4	0.72992	0.50000	0.12078	1.000
O1	0.39820	0.00000	0.10337	1.000
O2	0.89820	0.50000	0.10337	1.000
O3	0.07330	0.00000	0.09581	1.000
O4	0.57330	0.50000	0.09581	1.000
O5	0.75955	0.00000	0.06304	1.000
O6	0.25955	0.50000	0.06304	1.000
O7	0.90796	0.00000	0.26731	1.000
O8	0.40796	0.50000	0.26731	1.000
O9	0.20296	0.00000	0.26731	1.000
O10	0.70296	0.50000	0.26731	1.000
O11	0.97854	0.00000	0.35080	1.000
O12	0.47854	0.50000	0.35080	1.000
O13	0.61452	0.00000	0.47283	1.000
O14	0.11452	0.50000	0.47283	1.000

* Rwp = 11.34%, Rp = 9.17%

Table S3. Electrochemical performance of vanadium-based electrodes for magnesium battery.

Materials	Electrolyte	Capacity	Reference
V_2O_5/polyaniline	APC/1.0 M LiCl	361 mAh g^{-1} / 20 mA g^{-1}	1
NaV_6O_{15}	0.5 M $Mg(ClO_4)_2$/AN	213.4 mAh g^{-1} / 10 mA g^{-1}	2
Ti-V_2O_{5-x}	0.5 M $Mg(ClO_4)_2$/AN	241.3 mAh g^{-1} / 100 mA g^{-1}	3
NaV_3O_8	0.5 M $Mg(ClO_4)_2$/AN	260 mAh g^{-1} / 50 mA g^{-1}	4
$V_5O_{12}{\cdot}nH_2O$	0.3 M $Mg[N(SO_2CF_3)_2]_2$ /AN	160 mAh g^{-1} / 50 mA g^{-1}	5
V_2O_5- polyaniline	0.3 M $Mg(TFSI)_2$/AN	275 mAh g^{-1} / 100 mA g^{-1}	6
$Mg(Mg_{0.5}V_{1.5})O_4$	0.3 M $Mg(TFSI)_2$/AN	250 mA h g^{-1} / 100 mA g^{-1}	7
L-V_2O_5	0.3 M $Mg(TFSI)_2$/AN	355.3 mA h g^{-1} / 0.1 A g^{-1}	This Work
L-V_2O_5	MTB	157.1mA h g^{-1} / 0.1 A g^{-1}	This Work

Table S4. Ion diffusion coefficients of recently reported vanadium-based electrodes for magnesium battery.

Materials	D (cm^2 s^{-1})	Battery type	Reference
V_2O_5/PANI	10^{-17}-10^{-13}	Magnesium Battery	1
NaV_6O_{15}	7.55×10^{-13}-2.41×10^{-11}	Magnesium Battery	2
Ti-V_2O_{5-x}	10^{-14}-10^{-12}	Magnesium Battery	3
NaV_3O_8	6.45×10^{-15}-2.25×10^{-10}	Magnesium Battery	4
L-V_2O_5	2.32×10^{-11}-2.89×10^{-13}	Magnesium Battery	This Work

References

[1] J. Yang, X. W. Miao, C. R. Zhang, J. H. Zheng, C. C. Sun, Y. Zhang, H. B. Geng, *ChemNanoMat* **2022**, 8, e202200025

[2] D. Z. Wu, J. Zeng, H. M. Hua, J. N. Wu, Y. Yang, J. B. Zhao, *Nano Res.* **2020**, 13, 335.

[3] D. Z. Wu, Y. C. Zhuang, F. Wang, J. Zeng, J. B. Zhao, Y. Yang, *Nano Res.* **2023**, 16, 4880.

[4] H. Tang, F. Y. Xiong, Y. L. Jiang, C. Y. Pei, S. S. Tan, W. Yang, M. S. Li, Q. Y. An, L. Q. Mai, *Nano Energy* **2019**, 58, 347.

[5] Y. P. Zhu, G. Huang, J. Yin, Y. J. Lei, A. H. Emwas, X. Yu, O. F. Mohammed, H. N. Alshareef, *Adv. Energy Mater.* **2020**, 10, 2002128.

[6] C. L. Zuo, Y. Xiao, X. J. Pan, F. Y. Xiong, W. W. Zhang, J. C. Long, S. J. Dong, Q. Y. An, P. Luo, ChemSusChem 2021, 14, 2093.

[7] C. L. Zuo, W. Tang, B. X. Lan, F. Y. Xiong, H. Tang, S. J. Dong, W. W. Zhang, C. Tang, J. T. Li, Y. S. Ruan, S. B. Xi, Q. Y. An, P. Luo, *Chem. Eng. J.* **2021**, 405, 127005.